Comparison of SIA defect morphologies from different interatomic potentials for collision cascades in W

Bhardwaj, Utkarsh

Comparison of SIA Defect Morphologies from Different Interatomic Potentials for Collision Cascades in W

Utkarsh Bhardwaj[1]‡**, Andrea E. Sand**[2,3] **and Manoj Warrier**[1,4]

[1] Computational Analysis Division, BARC, Vizag, AP, India-530 012

[2] Department of Physics, P.O. Box 43, FI-00014 University of Helsinki, Finland

[3] Department of Applied Physics, Aalto University, FI-00076 Aalto, Espoo, Finland

[4] Homi Bhabha National Institute, Anushaktinagar, Mumbai, Maharashtra, India - 400 094

Abstract. The morphology of defects formed in collision cascades is an essential aspect of the subsequent evolution of the microstructure. The morphological composition of a defect decides its stability, interaction, and migration properties. We compare the defect morphologies in the primary radiation damage caused by high energy collision cascades simulated using three different interatomic potentials in W. An automated method to identify morphologies of defects is used. While most defects form $1/2\langle 111\rangle$ dislocation loops, other specific morphologies include $\langle 100\rangle$ dislocation loops, multiple loops clustered together, rings corresponding to C15 configuration and its constituent structures, and a combination of rings and dislocations. The analysis quantifies the distribution of defects among different morphologies and the size distribution of each morphology. We show that the disagreement between predictions of the different potentials regarding defect morphology is much stronger than the differences in predicted defect numbers.

Submitted to: *Modelling Simul. Mater. Sci. Eng.*

‡ butkarsh@barc.gov.in

1. Introduction

Predictive simulations of irradiation effects on material properties can be divided into two broad multi-scale studies: (i) Modeling the change in the microstructure of materials due to irradiation and (ii) Modeling the change in material properties due to the change in the microstructure. The first step in modeling the microstructure change is quantifying the number of defects, their spatial and size distributions, and classifying the defect cluster morphologies due to collision cascades initiated by energetic primary knock-on atoms (PKA). This information can then be used as input to higher scale simulations that model the migration, interaction and morphological evolution of these defects [1, 2, 3, 4, 5, 6, 7, 8, 9, 10, 11]. The morphology of a defect and the arrangement of its constituent components influence its thermal stability, migration properties, and interaction with other defects. Therefore it is necessary to classify the different possible defect morphologies occurring during primary damage in order to simulate micro-structure evolution.

Molecular dynamics (MD) simulations are widely used to simulate the primary damage caused by collision cascades [12, 13, 14, 15, 16, 17]. MD simulations give a good insight into the atomistic mechanisms of defect formation and clustering. They have been used to propose new formulae for the number of defects created based on physically realistic damage models [18]. In addition to the defect concentration, size distribution of point defect clusters and percentage of point defects in clusters have also been widely studied [15, 19]. The initial studies of defect morphologies were limited to the qualitative assessment of defects produced [20, 6] and their properties [8, 11]. With the increase in simulation data and automatic data-driven techniques, it is now possible to identify the morphology of all the defects produced and analyze them quantitatively [21, 22]. MD simulations can use different interatomic potentials developed for the same material. The assessment of variability in simulation results arising from the choice of different potentials is an essential step to determine the uncertainty of results before using them in higher scale models [20, 23].

The number of surviving point defects produced in W collision cascades shows notable variation across different interatomic potentials [24, 25]. The comparative study of W inter-atomic potentials by Sand et al. [24] shows that for energies up to 50 keV, the number of point defects correlates well with the threshold displacement energy and the form of potential in the short-range repulsive part. However, for higher energy cascades, the number of surviving point defects has been shown to only correlate well with the size of clusters formed for different interatomic potentials. Another earlier study by Sand et. al. [26] uses individual inspection guided by potential energy analysis to report qualitative differences in dislocation loops produced with different interatomic potentials in W at 150 keV. The study shows that for the potential by Derlet et al. [27], half of the smaller loops have Burgers vector $1/2\langle 111 \rangle$ and other half have $\langle 100 \rangle$, whereas half of all the larger clusters formed complex sessile configurations with sometimes visible partial loops. With the Ackland-Thetford EAM potential [28], all the clusters having

more than size 30 formed loops with $1/2\langle 111\rangle$ Burgers vector with the exception of one $\langle 100\rangle$ loop. Experiments have verified the presence of both $\langle 111\rangle$ and $\langle 100\rangle$ loops [29]. A later study by Wahyu et al. [25] using the Ackland-Thetford potential, finds similar morphologies with clusters bigger than size 30 mostly forming $\langle 111\rangle$ loops while all the clusters with size less than 30 are classified as 3D clusters that do not form loops. The study also shows a few $\langle 100\rangle$ loops, mixed loops, and 3D clusters of sizes greater than 30. The exact morphology of 3D clusters is not clear. The qualitative differences in defect morphologies formed with the different potentials and the presence of complex configurations or ambiguous 3D clusters demand a closer quantitative assessment of the defect morphologies formed with various potentials in W. Quantitative analysis of defect morphologies, other than giving essential insights into the radiation damage at atomistic scales, also helps in (a) providing inputs to higher scale models, (b) understanding the sessile/glissile nature of different defects, (c) understanding the interaction between different defect types (d) understanding their stability and morphological transitions, and (e) development of interatomic potentials that result in the defect morphologies that are consistent with experiments and Density Functional Theory (DFT) based studies [30, 31].

We present a comparative study of interatomic potentials of W based on the defect morphology formed in the high energy collision cascades. The method is applied to study and compare point defect clusters formed in W collision cascades at 100 keV and 200 keV using three different potentials. The potentials include the Finnis-Sinclair potential [32] as modified by Juslin et al. [33] (JW), potential by Derlet et al. [27] with the repulsive part fitted by Björkas et al. [34] (DND-BN), and the EAM4 potential by Marinica et al. [35], stiffened for cascade simulations (version denoted as M-S_h) by Sand et al. [24] (M-S). The three potentials have been earlier compared for other parameters such as defect count, and cascade evolution behavior [24]. The aim of this study is to classify the various defect morphologies that are formed in collision cascades in W resulting from three widely used interatomic potentials and discuss the differences in results from these potentials with regard to cluster morphologies. The current methods to study defect structures include the DXA algorithm [36], traditional geometrical methods such as common neighbor analysis, newer machine learning and statistical methods based on geometrical features, and a recent computational graph theory based algorithm, SaVi [22]. The DXA algorithm is a well-established method for dislocation analysis. However, it is limited to identifying only dislocations of significant sizes, and it also becomes increasingly slow as the number of atoms increase. The traditional geometrical methods, such as common neighbor analysis and centrosymmetric parameter, characterize the damaged region and atoms into known crystal geometries but do not find defect morphologies. A recent unsupervised machine learning method used simple geometrical features of angular and distance histograms [21] to identify various shapes automatically but failed to resolve components in a mixed morphology. Another statistical feature-based approach has been recently applied to identify C15 phases in Fe [37]. There are also some more new geometrical feature-based methods [38] that look promising, but the

extent of their accuracy and efficiency is not yet clear. The morphological analysis in the current work is done using SaVi algorithm, which resolves every point defect cluster into its homogeneous constituent components and characterizes them [22]. The method identifies the dislocation loops with their Burgers vector orientation and magnitude even in the complex clusters of mixed dislocations and rings. It also identifies C15-like rings and can be extended to other specific arrangements of the dumbbells/crowdions. The method also gives the internal morphological details, such as each crowdion's exact orientation and length. Using the method, we classify the defect morphologies into dislocation loops with their Burgers vector orientation, C15 like 3D rings and their basis structures [39, 40, 22] that also form independent defects, mixed dislocation loops with details of their constituent loops, and defects composed of both ring and dislocation loops. We compare the distribution of defects in different cluster morphologies and the size distribution of each morphology separately. We show that the disagreement between predictions of the different potentials regarding defect morphology is more substantial than the differences in predicted defect numbers.

2. Methods

The MD simulations of collision cascades for 100 and 200 keV PKA were performed using the PARCAS MD code [41]. A primary knock-on atom (PKA) was selected from among the lattice atoms of a cubic simulation cell and given the desired kinetic energy in a random initial direction. Periodic boundaries were used for each cascade. Simulations in which atoms with kinetic energy above 10 eV crossed any of the periodic boundaries were aborted, and the initial position of the recoil was shifted further from the border. Temperature control at 0K was applied to all atoms within three atomic layers from the cell borders using a Berendsen thermostat [42]. Each cascade was followed until the cell had cooled to an average temperature of only a few K, ensuring stable defects. Electronic stopping was considered, with a lower velocity cutoff of 10 eV, using the stopping power tables from SRIM [43].

The defect morphology identification is carried out using SaVi algorithm, a recent computational graph [44] based morphology identification method [22, 45]. The method resolves the homogeneous constituent components of a defect and characterizes it based on the morphology of the components. This enables a clear definition of mixed morphology defects. A component comprises dumbbells/crowdions that hold a specific relationship with their neighboring dumbbells/crowdions. The method identifies various properties of dumbbells/crowdions, such as their extents, orientations, distances, and angles with neighbors to identify and characterize the components. For example, the angle of neighboring dumbbells/crowdions in a dislocation loop is close to zero, while in a C15 like ring, it is sixty degrees. The method identifies the Burgers vector direction and magnitude of each component loop in a defect. It also can classify a C15 like a ring and its constituent basis shapes even in the presence of a trapped dislocation loop. The method can be extended to identify any specific defect geometry and different materials.

3. Results

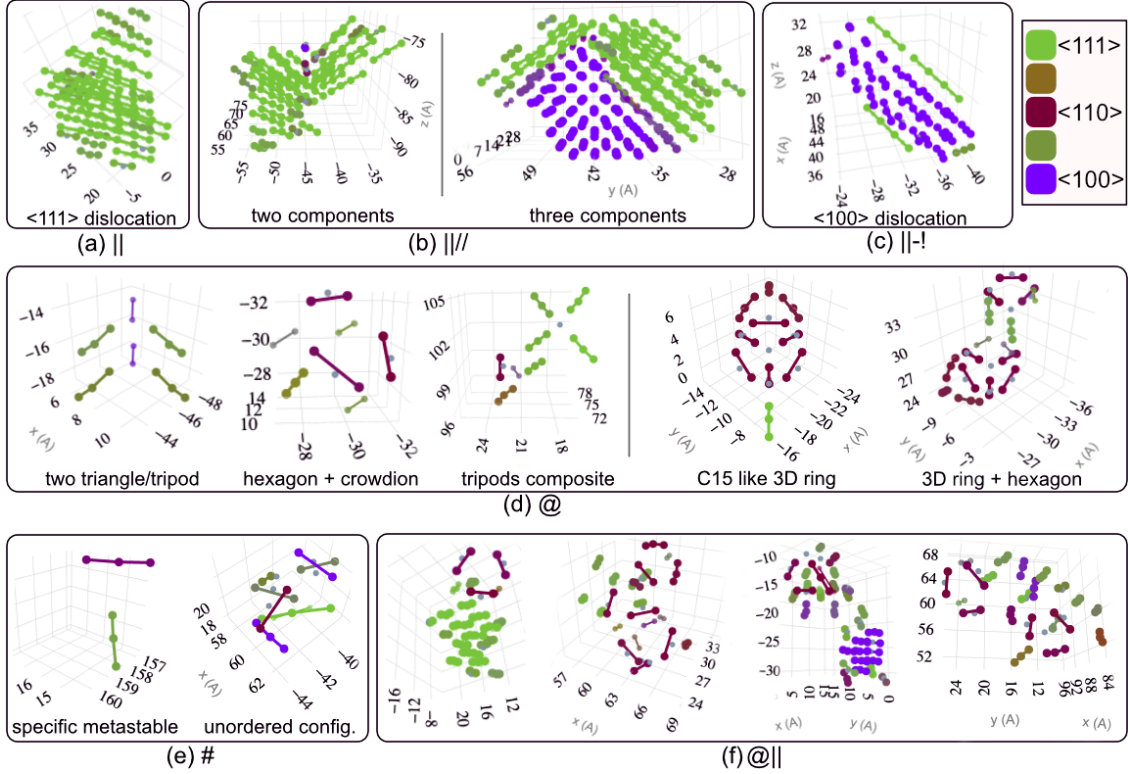## 3.1. Defect Morphologies in W collision cascades

Figure 1. Defect morphology formed in the W collision cascades along with the symbols used to represent them. (a) parallel bundle of ⟨111⟩ directed SIA that form $1/2\langle111\rangle$ edge dislocation loop, (b) defects composed of multiple dislocation loops (here three loops, 2 in ⟨111⟩ and 1 in ⟨100⟩ direction), (c) parallel group of ⟨100⟩ directed SIA that form ⟨100⟩ loop, (d) 3D C15 like rings and their constituent basis, (e) non-parallel and non-ring configurations (f) defects with dislocations trapped with rings (here hexagonal planar ring along with ⟨111⟩ loop). Lines are drawn along the dumbbells/crowdions and are colored according to their orientation as specified in the legend (top-right).

Figure 1 shows the different morphologies found in the W collision cascades. A bundle of parallel dumbbells/crowdions form a dislocation loop with Burgers vector direction similar to the dumbbells/crowdions orientation. The first three morphologies in (a), (b), and (c) are formed of dislocation loops. The ⟨100⟩ loop almost always exhibits a few ⟨111⟩ crowdions on the periphery, as shown in (c). Multiple dislocation loops compose together to form a sessile defect. Another stable sessile defect morphology is C15-like ring morphology, as shown in (d). The constituent basis structures that a C15 ring is composed of, viz. triangle/tripod and hexagonal ring can exist as a separate stable sessile defect [39, 40, 21, 22]. A pair of orthogonal dumbbells/crowdions is another specific structure that is observed relatively rarely (the first defect in Figure 1 (e)). A small fraction of defects also settle down transiently in a configuration with no specific order of dumbbells/crowdions (the second defect in Figure 1 (e)). These are primarily non-recurring transient variations of parallel or sometimes ring morphologies appearing

different due to thermal vibrations. A defect can be composed of both a dislocation loop and a ring, as shown in Figure 1 (f).

Table 1. Description and ASCII symbol for different cluster morphologies.

Symbol	Description
||	Parallel bundle (dislocations) in $\langle 111 \rangle$ orientation
||−!	Parallel bundle (dislocations) in $\langle 100 \rangle$ orientation (having $\langle 111 \rangle$ crowdions on fringes)
||//	Multi-component dislocations
@	Rings, (C15-like or its basis shapes)
@||	Composed of both, rings & dislocations
#	Non-parallel & non-ring configurations

Table 1 lists the different morphologies and the symbol used to represent them. The symbols are chosen such that they indicate the morphology.

3.2. Distribution of defects in different cluster morphologies

The kind of defect morphologies found for all the three interatomic potentials are broadly the same. The morphologies include dislocation loops in $\langle 111 \rangle$ and $\langle 100 \rangle$ orientations, rings corresponding to C15-like configuration and its constituent basis, and a few non-parallel and non-ring transient configurations. However, the proportions and sizes of the morphologies differ substantially.

The M-S potential shows more preference for forming rings as opposed to DND-BN and JW that prefer components composed of parallel crowdions and dumbbells (Figure 2 b). The components composed of parallel crowdions and dumbbells form the dislocation loops with a Burgers vector orientation that is the same as the orientation of the constituent dumbbells/crowdions [22]. DND-BN shows a greater preference for multi-component dislocation loops (\|\|//) than JW potential which prefers $\langle 111 \rangle$ dislocation loops (\|\|) (Figure 2 c-i, c-ii).

The M-S potential also shows a different trend for the fraction of defects forming \|\| for the two energies explored. The fraction of defects forming \|\| morphology is lesser at 200 keV than in 100 keV for both JW and DND-BN but not for M-S (Figure 2 c-i). The overall fraction in parallel components is still more at 200 keV for all the three potentials (Figure 2 b). The drop in the \|\| and \|\|−! morphology in DND-BN and JW at 200 keV is compensated by the stark increase in \|\|// morphology (Figure 2 b-ii).

The DND-BN potential shows a very distinctive preference for the multi-component (\|\|//) dislocation morphology which increases further at 200 keV (Figure 2 b-ii). Figure 3 plots the number of components and their sizes in the \|\|// morphology for all the potentials. For example, there are two defects that are composed of four dislocations shown as black triangles for a x-axis value of 4. The eight dots for the same x-axis value represent the eight dislocation components for the two defects (four each). The
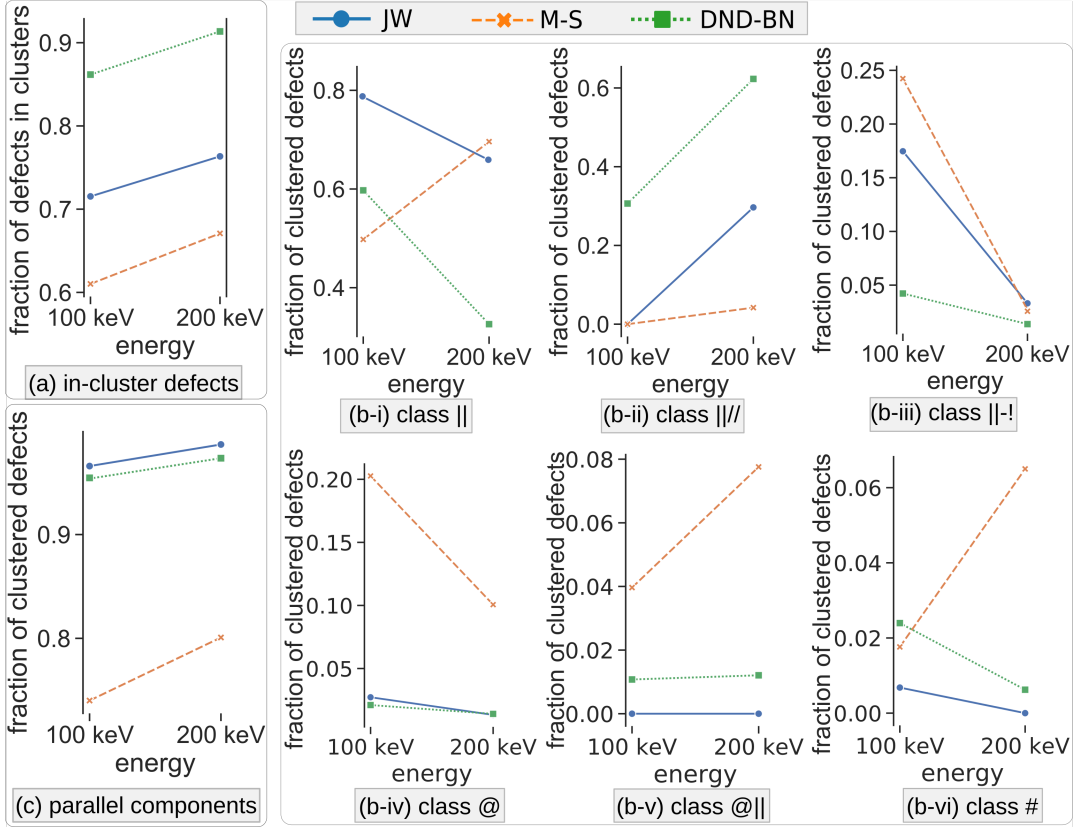
Figure 2. (a) Shows the fraction of point defects in clusters for the three potentials (represented by different styles and colors; blue: JW, orange: M-S, green: DND-BN). The fraction increases with energy for all the three potentials (b) shows the distribution of the in-cluster defects in different morphologies viz. (i) glissile single parallel SIAs component in ⟨110⟩ orientation (||), (ii) multiple parallel components (||//) (iii) single parallel component in ⟨111⟩ orientation (||−!), (iv) rings (@), (v) parallel and ring combination (@||), (vi) non-parallel, non-ring configurations (#). The cluster shapes for different morphologies are shown in Figure 1. (c) shows the fraction of in-cluster defects in parallel components that form dislocation loops. These include single dislocations in ⟨111⟩ and ⟨100⟩ directions as well as multi-component dislocations. The fractions in (b) and (c) are calculated with respect to the total in-cluster defects.

size on the y-axis corresponds to the surviving number of point defects. The values show that the ||// morphology is vastly different in structural composition from single dislocations. This further emphasizes the significance of the relatively higher preference for ||// morphology with DND-BN potential.
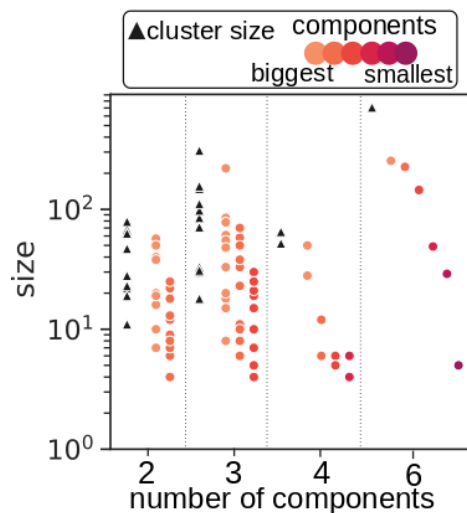
Figure 3. The number of components and their sizes for multi-component dislocation loops (||//) found using all the potentials. The DND-BN potential shows a distinctive preference for this morphology compared to the other two potentials (Figure 2 (b-ii)). The x-axis shows the count of the components such that all the clusters with the same number of components are plotted together. The components are arranged in descending order of their sizes and are represented with a color gradient.

The structure of 3D rings corresponds to the C15 symmetry, as shown in Figure 4. Out of all the rings for each potential, less than 10% are C-15 like 3D rings, while most of the rings are planar hexagonal and triangle/tripod morphologies.
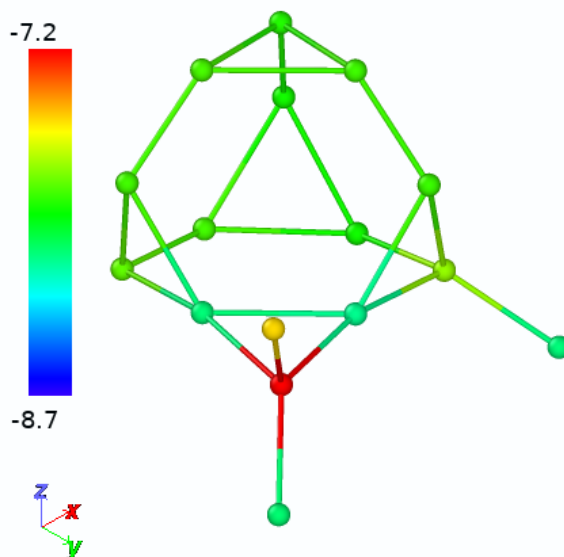

Figure 4. A cluster found at 100keV showing a C15 like structure consisting of four hexagons joined at 12 vertices forming a Laves Polyhedron with a crowdion tail appended to it. The color map shows the potential energy of the atoms.

Table 2 and Table 3 list the distribution of the absolute number of point defects and

defect clusters, respectively. Note that the number of cascades is different for different potentials and energies in the data-set, and the absolute numbers must be compared, keeping the number of cascades in context. The relative numbers per cascade have been shown in Figure 2 earlier. The number of clusters formed for each potential is well above 100. The total number of clusters is 574.

Table 2. Distribution of absolute number of point defects. E_{pka} is in keV.

Potential	E_{pka}	cascades	$\|\|$	$\|\|-!$	$\|\|//$	@	@$\|\|$	#	total
JW	100	5	242	42	0	8	0	2	294
	200	5	459	11	202	9	0	0	681
M-S	100	5	113	55	0	46	9	4	227
	200	5	296	45	20	48	37	31	477
DND-BN	100	20	1226	109	622	43	22	23	2045
	200	9	845	50	1584	36	31	16	2562

Table 3. Distribution of absolute number of defect clusters. E_{pka} is in keV.

	E_{pka}	cascades	$\|\|$	$\|\|-!$	$\|\|//$	@	@$\|\|$	#	total
JW	100	5	34	2	0	4	0	1	41
	200	5	76	1	2	4	0	0	83
M-S	100	5	40	2	0	14	2	1	59
	200	5	61	2	1	20	4	5	93
DND-BN	100	20	127	5	15	11	3	9	170
	200	9	92	2	11	14	3	6	128

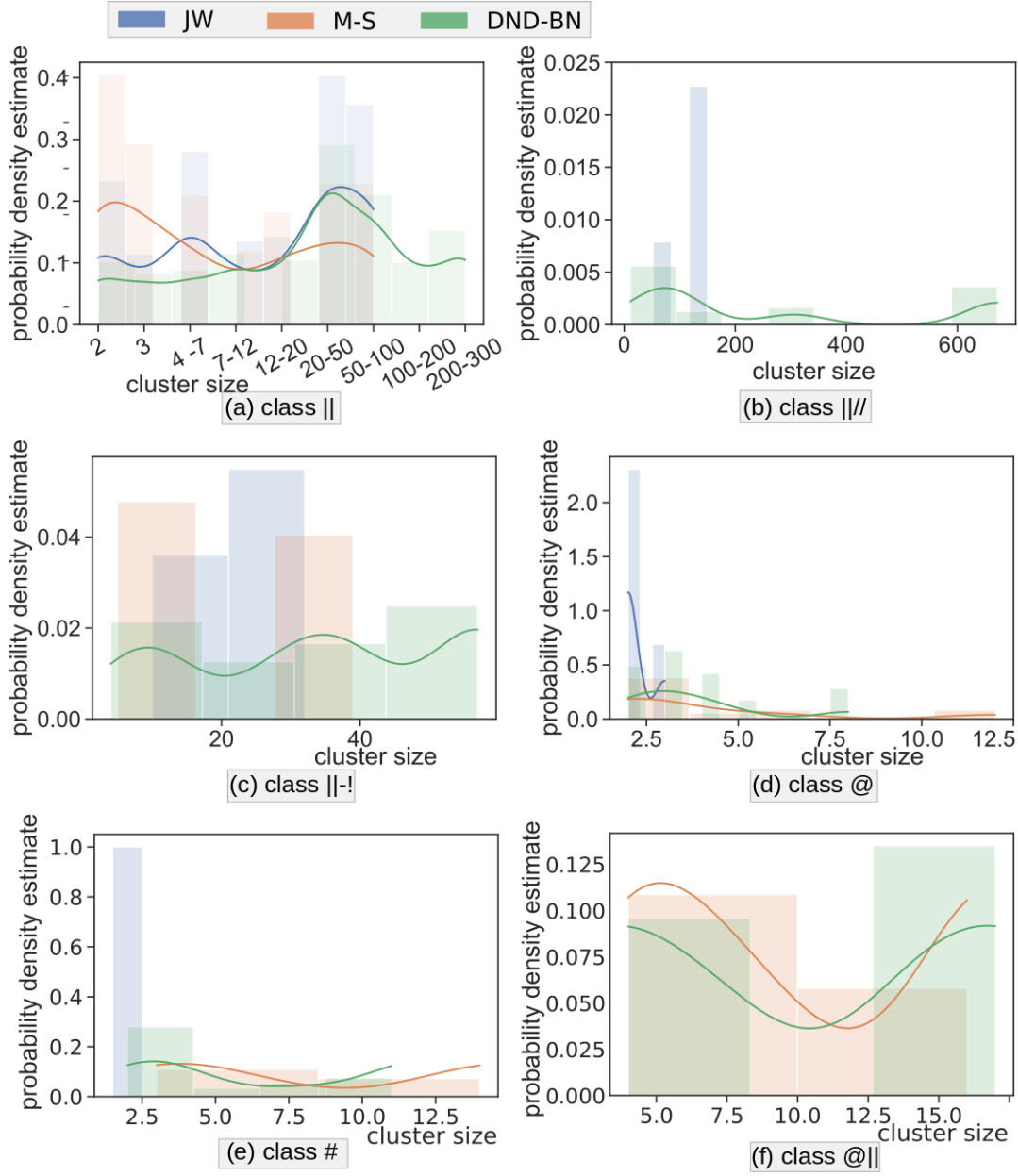*3.3. Cluster size distribution across cluster morphologies*

Figure 5. Cluster size distribution for a different class of morphologies. The y-axis shows the probability density for different defect sizes marked on the x-axis. The bars and curves show histogram bin values and probability estimates, respectively. Different potentials are shown with different colors. The curves are only drawn for cases with sufficient data. The kernel density estimation curves are found using the Gaussian kernel with bandwidth suggested by Scott's rule [46]. The width of the bar represents the bin size. The bin sizes are calculated using Freedman Diaconis Estimator [47] to bring out the relative comparison in the plots.

Figure 5 shows the size distribution of defects for different morphologies. The values are probability density estimates for each potential. In general, the defects with non-

parallel morphology are small when compared to the parallel dislocations ((a), (b), and (c) Figure 5). The DND-BN potential has large clusters with parallel components in classes ||, ||−! and especially ||//. The biggest cluster is formed with six parallel components, out of which three are oriented in ⟨110⟩ and three in ⟨111⟩.

For the M-S potential, most of the clusters in the || class are of size two. For non-parallel classes, the size distribution is spread out. For JW potential, there are no unordered arrangements, the only cluster that appears in class #, is a pair of orthogonal dumbbells(the first defect in Figure 1 (e)). For class @ in JW, mostly all the defects are of size two while a few also have size three.

3.4. Deviation from primary alignments and lattice site non-collinearity

For a single SIA dumbbell or crowdion, or for parallel bundles of dumbbells and crowdions, it is expected that the lattice site is collinear with the line that passes through the two SIA atoms that co-occupy it. The SIA dumbbell/crowdion is normally characterized as aligned to one of the primary orientations ⟨110⟩, ⟨100⟩ or ⟨111⟩. Recent DFT studies show that an SIA adopts a symmetry-broken configuration in chromium, molybdenum, and tungsten [48]. For non-parallel dumbbell configurations like basis of rings such as tripod, we observe that many of the crowdions are aligned slightly off from these standard orientations. The slight deviations from the standard orientations are expected to be present due to thermal vibrations. However, it is interesting to observe the relative differences in the statistical distribution of deviations obtained with the different potentials. Since there are multiple dumbbells/crowdions in a single point defect cluster, the total number of dumbbells/crowdions is sufficient for drawing a statistically valid comparison of the distributions.

Figure 6 shows these two deviations viz. lattice-point non-collinearity and deviation from perfect crowdion orientation for the different classes and potentials. The lattice-point non-collinearity value is taken as the perpendicular distance (in Å) of the lattice point from the line defined by the two interstitials occupying it. The angular deviation from perfect crowdion orientation is normalized by dividing the angle with the maximum value of deviation observed for the data, i.e., 30 degrees.

The deviation in orientation is least in parallel ⟨110⟩ clusters (||), followed by ||−! and ||//. For non-parallel random orientation class (#) plotted in (d), the deviation is large. The non-collinearity of lattice point follows the same trend, except ||// has slightly higher values than ||−!. The deviation in orientation seems to be depending on the orientation of the SIA, with the least deviation in morphologies with ⟨110⟩ orientations, followed by ⟨111⟩ and ⟨100⟩. The non-collinearity can be viewed as increasing with the increase in SIAs having non-parallel neighborhood. For ||//, non-parallel SIAs are present where two components are interfaced, however in ||−! it occurs when the ⟨111⟩ SIAs that are in main component are interfaced with surrounding non-parallel SIAs on the fringes.

Among potentials, JW shows the lowest deviations, especially for ⟨110⟩ dislocation
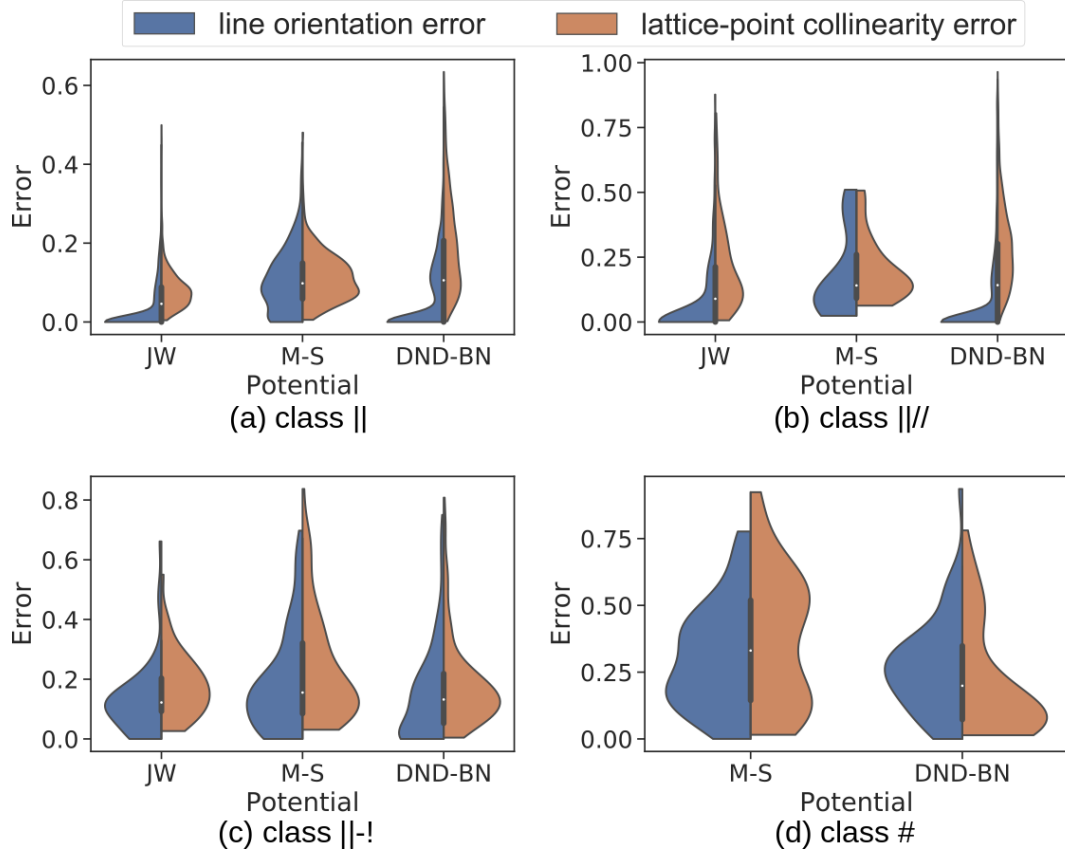
Figure 6. Statistical distribution of lattice point non-collinearity (red) and deviation from primary orientation (blue) for different classes across potentials. The deviations are lower for classes where parallel SIAs are more. For non-parallel random orientation class (#) plotted in (d), the deviations are large as expected. Among potentials JW shows the lowest deviations especially for $\langle 110 \rangle$ dislocation loops (||).

loops (||). This behavior by JW is consistent with a strong preference for clusters with parallel SIAs and almost negligible preference for another arrangement of SIAs except for small di-interstitials, be it @ or #.

4. Discussion

The energy available for defect formation during the collision cascade far exceeds the formation energy of any quasi-stable defects in the observed cluster-size range. Defect formation within the heat spike region [49] thus becomes a question of the available time and transition pathways from the disordered liquid-like state to the various lower energy configurations of defects or perfect crystal. All interatomic potentials in this study are found to produce a fraction of defect clusters which differ from the predicted lowest energy defect configurations. The validity of this general result is supported by experimental evidence indicating that $\langle 100 \rangle$ dislocation loops form directly as a result of cascades in W, despite being energetically unfavorable with respect to $\langle 111 \rangle$ loops [50].

The relaxation process of the cascade core depends on the recrystallization rate as well as on details of the potential energy landscape. From this perspective, the M-S potential, which has been fitted using liquid configurations in addition to perfect crystal and point defects, may capture the relaxation process more accurately. Thus, the prediction of a relatively high number of small C15-like structures in the primary damage according to M-S may be significant and deserves further study, despite the fact that the C15 phase is energetically unfavorable in tungsten [51]. On the other hand, the M-S potential predicts a melting point far in excess of the experimental melting point of tungsten [24], and this has a strong impact on the recrystallization rate [52], which may in turn lead to incorrect predictions. In addition, the pronounced lack of large dislocation loops in the damage predicted by the M-S potential appears to contradict experiment, where impacts of 150 keV W ions are found to directly produce defects, up to sizes of a few nanometers in diameter [50] which can be identified using a Transmission Electron Microscopy (TEM).

It is possible that real materials behave according to a blend of the predictions of these different potentials. Since cascade-induced defects do not necessarily form in lowest energy configurations, the predictions of the cascade damage formation process cannot be validated through comparison with low-energy defect structures computed e.g. with DFT. Resolving the question of the accuracy of the various potentials for cascade simulations most likely hinges on obtaining parameters suggested by each potential to carry out higher scale simulations, coupled with developments in the resolution of experimental imaging techniques, since most of the clusters formed in-cascade are below the observational limit of conventional transmission electron microscopy [49].

5. Conclusions

We have used a novel computational method based on graph theory to characterize the defect cluster morphologies in the primary radiation damage in tungsten as predicted by molecular dynamics simulations. The newly developed analysis method provides a detailed characterization of the morphology-based on the constituent homogeneous components of the defect clusters. We have applied the method to classify the morphologies of defects formed at energies of 100 keV and 200 keV, comparing the predictions of three different interatomic potentials.

We find a marked difference in the predicted morphology of the primary damage simulated with the different potentials. In particular, we note that the JW potential displays the strongest tendency to form ideal dislocation loops with single Burgers vectors of either $\langle 111 \rangle$ or $\langle 100 \rangle$ direction, whereas the DND-BN potential additionally predicts the frequent formation of very large multi-component loops, where different parts have different Burgers vectors. The M-S potential, on the other hand, predicts a large fraction of defects that do not display a dislocation loop character, but rather contain components of 2D or 3D rings, including small clusters with a C15 structure. These clusters are typically much smaller than the well-formed dislocation loops, and

would be below the resolution limit of TEM.

In line with the observation of the tendency to form well resolved defects, we also find that the JW potential predicts constituent SIA configurations most closely aligned with the bcc lattice positions. Nevertheless, all potentials show the formation of defect clusters with morphologies different from that which can be expected based solely on a minimum formation energy criteria for the respective potential.

The detailed investigation of the morphological structure presented here provides a rigorous comparison of the predictions of different interatomic potentials going beyond the conventional measure of the point defect count. Applied to larger databases, such as that currently being developed by the IAEA containing cascade damage configurations in various materials [53, 54], this method can serve to inform larger-scale models designed to treat radiation damage evolution on longer time scales, where the morphology of defects has a significant impact on the stability, interaction and mobility of defects. As such, this work demonstrates a valuable tool in the ongoing effort to formulate multi-scale models of radiation effects in materials with increasing accuracy and predictive power.

References

[1] H. L. Heinisch, B. N. Singh, Molecular dynamics and binary collision modeling of the primary damage state of collision cascades, Journal of nuclear materials 191 (1992) 1083–1087.

[2] C. S. Becquart, M. Hou, A. Souidi, The primary damage in Fe revisited by molecular dynamics and its binary collision approximation, MRS Online Proceedings Library Archive 650.

[3] A. Souidi, M. Hou, C. Becquart, C. Domain, Atomic displacement cascade distributions in iron, Journal of Nuclear Materials 295 (2) (2001) 179 – 188. doi:10.1016/S0022-3115(01)00556-6.

[4] L. Bukonte, F. Djurabekova, J. Samela, K. Nordlund, S. A. Norris, M. J. Aziz, Comparison of molecular dynamics and binary collision approximation simulations for atom displacement analysis, Nuclear Instruments and Methods in Physics Research Section B: Beam Interactions with Materials and Atoms 297 (2013) 23–28.

[5] A. De Backer, A. Sand, C. J. Ortiz, C. Domain, P. Olsson, E. Berthod, C. S. Becquart, Primary damage in tungsten using the binary collision approximation, molecular dynamic simulations and the density functional theory, Physica Scripta 2016 (T167) (2016) 014018.

[6] D. Bacon, F. Gao, Y. Osetsky, The primary damage state in fcc, bcc and hcp metals as seen in molecular dynamics simulations, Journal of Nuclear Materials 276 (1) (2000) 1 – 12. doi:https://doi.org/10.1016/S0022-3115(99)00165-8.
URL http://www.sciencedirect.com/science/article/pii/S0022311599001658

[7] B. Singh, S. Golubov, H. Trinkaus, A. Serra, Y. Osetsky, A. Barashev, Aspects of microstructure evolution under cascade damage conditions, Journal of Nuclear Materials 251 (1997) 107 – 122, proceedings of the International Workshop on Defect Production, Accumulation and Materials Performance in an Irradiation Environment. doi:https://doi.org/10.1016/S0022-3115(97)00244-4.
URL http://www.sciencedirect.com/science/article/pii/S0022311597002444

[8] Y. Osetsky, D. Bacon, A. Serra, B. Singh, S. Golubov, Stability and mobility of defect clusters and dislocation loops in metals, Journal of Nuclear Materials 276 (1) (2000) 65 – 77. doi:https://doi.org/10.1016/S0022-3115(99)00170-1.
URL http://www.sciencedirect.com/science/article/pii/S0022311599001701

[9] C. Becquart, A. Souidi, C. Domain, M. Hou, L. Malerba, R. Stoller, Effect of displacement cascade

structure and defect mobility on the growth of point defect clusters under irradiation, Journal of Nuclear Materials 351 (1) (2006) 39 – 46, proceedings of the Symposium on Microstructural Processes in Irradiated Materials. doi:https://doi.org/10.1016/j.jnucmat.2006.02.022.
URL http://www.sciencedirect.com/science/article/pii/S002231150600064X

[10] Y. Osetsky, D. Bacon, B. Singh, B. Wirth, Atomistic study of the generation, interaction, accumulation and annihilation of cascade-induced defect clusters, Journal of Nuclear Materials 307-311 (2002) 852 – 861. doi:https://doi.org/10.1016/S0022-3115(02)01094-2.
URL http://www.sciencedirect.com/science/article/pii/S0022311502010942

[11] F. Gao, D. Bacon, Y. Osetsky, P. Flewitt, T. Lewis, Properties and evolution of sessile interstitial clusters produced by displacement cascades in alpha-iron, Journal of Nuclear Materials 276 (1) (2000) 213 – 220. doi:https://doi.org/10.1016/S0022-3115(99)00180-4.
URL http://www.sciencedirect.com/science/article/pii/S0022311599001804

[12] J. B. Gibson, A. N. Goland, M. Milgram, G. H. Vineyard, Dynamics of radiation damage, Phys. Rev. 120 (1960) 1229–1253. doi:10.1103/PhysRev.120.1229.

[13] C. Erginsoy, G. H. Vineyard, A. Englert, Dynamics of radiation damage in a body-centered cubic lattice, Phys. Rev. 133 (1964) A595–A606. doi:10.1103/PhysRev.133.A595.
URL https://link.aps.org/doi/10.1103/PhysRev.133.A595

[14] C. Erginsoy, G. H. Vineyard, A. Shimizu, Dynamics of radiation damage in a body-centered cubic lattice. ii. higher energies, Phys. Rev. 139 (1965) A118–A125. doi:10.1103/PhysRev.139.A118.
URL https://link.aps.org/doi/10.1103/PhysRev.139.A118

[15] R. Stoller, 1.11 - primary radiation damage formation, in: R. J. Konings (Ed.), Comprehensive Nuclear Materials, Elsevier, Oxford, 2012, pp. 293 – 332. doi:https://doi.org/10.1016/B978-0-08-056033-5.00027-6.

[16] K. Nordlund, Molecular dynamics simulation of ion ranges in the 1–100 keV energy range, Computational materials science 3 (4) (1995) 448–456.

[17] W. Cai, J. Li, S. Yip, 1.09 molecular dynamics, Compr. Nucl. Mater., edited by JMK Rudy (Elsevier, Oxford, 2012) (2012) 249–265.

[18] K. Nordlund, S. J. Zinkle, A. E. Sand, F. Granberg, et al., Improving atomic displacement and replacement calculations with physically realistic damage models, Nature Communications 9 (2018) 1084.

[19] M. Warrier, U. Bhardwaj, H. Hemani, R. Schneider, A. Mutzke, M. Valsakumar, Statistical study of defects caused by primary knock-on atoms in fcc cu and bcc w using molecular dynamics, Journal of Nuclear Materials 467 (2015) 457–464.

[20] Y. Osetsky, D. Bacon, Defect cluster formation in displacement cascades in copper, Nuclear Instruments and Methods in Physics Research Section B: Beam Interactions with Materials and Atoms 180 (1) (2001) 85 – 90, computer Simulation of Radiation Effects in Solids. doi:https://doi.org/10.1016/S0168-583X(01)00400-1.
URL http://www.sciencedirect.com/science/article/pii/S0168583X01004001

[21] U. Bhardwaj, A. E. Sand, M. Warrier, Classification of clusters in collision cascades, Computational Materials Science 172 (2020) 109364. doi:https://doi.org/10.1016/j.commatsci.2019.109364.
URL http://www.sciencedirect.com/science/article/pii/S0927025619306639

[22] U. Bhardwaj, A. E. Sand, M. Warrier, Graph theory based approach to characterize self interstitial defect morphology, Computational Materials Science 195 (2021) 110474. doi:https://doi.org/10.1016/j.commatsci.2021.110474.
URL https://www.sciencedirect.com/science/article/pii/S0927025621001993

[23] J. Byggmstar, F. Granberg, K. Nordlund, Effects of the short-range repulsive potential on cascade damage in iron, Journal of Nuclear Materials 508 (2018) 530 – 539. doi:https://doi.org/10.1016/j.jnucmat.2018.06.005.
URL http://www.sciencedirect.com/science/article/pii/S0022311518305166

[24] A. Sand, J. Dequeker, C. Becquart, C. Domain, K. Nordlund, Non-equilibrium properties of

interatomic potentials in cascade simulations in tungsten, Journal of Nuclear Materials 470 (2016) 119 – 127. doi:https://doi.org/10.1016/j.jnucmat.2015.12.012.
URL http://www.sciencedirect.com/science/article/pii/S0022311515303810

[25] W. Setyawan, G. Nandipati, K. J. Roche, H. L. Heinisch, B. D. Wirth, R. J. Kurtz, Displacement cascades and defects annealing in tungsten, part i: Defect database from molecular dynamics simulations, Journal of Nuclear Materials 462 (2015) 329 – 337. doi:https://doi.org/10.1016/j.jnucmat.2014.12.056.
URL http://www.sciencedirect.com/science/article/pii/S0022311514009982

[26] A. E. Sand, S. L. Dudarev, K. Nordlund, High-energy collision cascades in tungsten: Dislocation loops structure and clustering scaling laws, EPL (Europhysics Letters) 103 (4) (2013) 46003. doi:10.1209/0295-5075/103/46003.
URL https://doi.org/10.1209%2F0295-5075%2F103%2F46003

[27] P. M. Derlet, D. Nguyen-Manh, S. L. Dudarev, Multiscale modeling of crowdion and vacancy defects in body-centered-cubic transition metals, Phys. Rev. B 76 (2007) 054107. doi:10.1103/PhysRevB.76.054107.
URL https://link.aps.org/doi/10.1103/PhysRevB.76.054107

[28] G. J. Ackland, R. Thetford, An improved n-body semi-empirical model for body-centred cubic transition metals, Philosophical Magazine A 56 (1) (1987) 15–30. doi:10.1080/01418618708204464.

[29] X. Yi, M. Jenkins, M. Briceno, S. Roberts, Z. Zhou, M. Kirk, In situ study of self-ion irradiation damage in w and w5re at 500c, Philosophical Magazine 93 (14) (2013) 1715–1738. doi:10.1080/14786435.2012.754110.
URL http://dx.doi.org/10.1080/14786435.2012.754110

[30] R. Alexander, M.-C. Marinica, L. Proville, F. Willaime, K. Arakawa, M. R. Gilbert, S. L. Dudarev, Ab initio scaling laws for the formation energy of nanosized interstitial defect clusters in iron, tungsten, and vanadium, Phys. Rev. B 94 (2016) 024103. doi:10.1103/PhysRevB.94.024103.
URL https://link.aps.org/doi/10.1103/PhysRevB.94.024103

[31] R. Alexander, L. Proville, C. S. Becquart, A. M. Goryeava, J. Drs, C. Lapointe, M.-C. Marinica, Interatomic potentials for irradiation-induced defects in iron, Journal of Nuclear Materials 535 (2020) 152141. doi:https://doi.org/10.1016/j.jnucmat.2020.152141.
URL http://www.sciencedirect.com/science/article/pii/S0022311520302014

[32] M. W. Finnis, J. E. Sinclair, A simple empirical n-body potential for transition metals, Philosophical Magazine A 50 (1) (1984) 45–55. doi:10.1080/01418618408244210.

[33] N. Juslin, B. Wirth, Interatomic potentials for simulation of he bubble formation in w, Journal of Nuclear Materials 432 (1) (2013) 61 – 66. doi:https://doi.org/10.1016/j.jnucmat.2012.07.023.
URL http://www.sciencedirect.com/science/article/pii/S0022311512003820

[34] C. Bjrkas, K. Nordlund, S. Dudarev, Modelling radiation effects using the ab-initio based tungsten and vanadium potentials, Nuclear Instruments and Methods in Physics Research Section B: Beam Interactions with Materials and Atoms 267 (18) (2009) 3204 – 3208, proceedings of the Ninth International Conference on Computer Simulation of Radiation Effects in Solids. doi:https://doi.org/10.1016/j.nimb.2009.06.123.
URL http://www.sciencedirect.com/science/article/pii/S0168583X09007575

[35] M.-C. Marinica, L. Ventelon, M. R. Gilbert, L. Proville, S. L. Dudarev, J. Marian, G. Bencteux, F. Willaime, Interatomic potentials for modelling radiation defects and dislocations in tungsten, Journal of Physics: Condensed Matter 25 (39) (2013) 395502. doi:10.1088/0953-8984/25/39/395502.
URL https://doi.org/10.1088%2F0953-8984%2F25%2F39%2F395502

[36] A. Stukowski, V. V. Bulatov, A. Arsenlis, Automated identification and indexing of dislocations in crystal interfaces, Modelling and Simulation in Materials Science and Engineering 20 (8) (2012) 085007. doi:10.1088/0965-0393/20/8/085007.

[37] A. M. Goryaeva, C. Lapointe, C. Dai, J. Dérès, J.-B. Maillet, M.-C. Marinica, Reinforcing materials modelling by encoding the structures of defects in crystalline solids into distortion scores, Nature communications 11 (1) (2020) 1–14.

[38] U. von Toussaint, F. Dominguez-Gutierrez, M. Compostella, M. Rampp, Favad: A software workflow for characterisation and visualizing of defects in crystalline structures, arXiv preprint arXiv:2004.08184.

[39] L. Dzerald, M.-C. Marinica, L. Ventelon, D. Rodney, F. Willaime, Stability of self-interstitial clusters with c15 laves phase structure in iron, Journal of Nuclear Materials 449 (1) (2014) 219 – 224. doi:https://doi.org/10.1016/j.jnucmat.2014.02.012.
URL http://www.sciencedirect.com/science/article/pii/S0022311514000749

[40] M.-C. Marinica, F. Willaime, J.-P. Crocombette, Irradiation-induced formation of nanocrystallites with $c15$ laves phase structure in bcc iron, Phys. Rev. Lett. 108 (2012) 025501. doi:10.1103/PhysRevLett.108.025501.
URL https://link.aps.org/doi/10.1103/PhysRevLett.108.025501

[41] K. Nordlund, Parcas computer code, the main principles of the molecular dynamics algorithms are presented in [58], The adaptive time step and electronic stopping algorithms are the same as in [19].

[42] H. J. C. Berendsen, J. P. M. Postma, W. F. van Gunsteren, A. DiNola, J. R. Haak, Molecular dynamics with coupling to an external bath, The Journal of Chemical Physics 81 (8) (1984) 3684–3690. arXiv:https://doi.org/10.1063/1.448118, doi:10.1063/1.448118.
URL https://doi.org/10.1063/1.448118

[43] J. F. Ziegler, Srim-2008.04 software package (2008).
URL http://www.srim.org

[44] R. Tarjan, Depth-first search and linear graph algorithms, SIAM Journal on Computing 1 (2) (1972) 146–160. doi:10.1137/0201010.
URL https://doi.org/10.1137/0201010

[45] U. Bhardwaj, H. Hemani, M. Warrier, N. Semwal, K. Ali, A. Arya, Csaransh: Software suite to study molecular dynamics simulations of collision cascades, Journal of Open Source Softwaredoi:10.21105/joss.01461.

[46] M. T. Goodrich, R. Tamassia, Algorithm Design and Applications, 1st Edition, Wiley Publishing, 2014.

[47] D. Freedman, P. Diaconis, On the histogram as a density estimator: L 2 theory, Zeitschrift für Wahrscheinlichkeitstheorie und verwandte Gebiete 57 (4) (1981) 453–476.

[48] P.-W. Ma, S. L. Dudarev, Symmetry-broken self-interstitial defects in chromium, molybdenum, and tungsten, Phys. Rev. Materials 3 (2019) 043606. doi:10.1103/PhysRevMaterials.3.043606.
URL https://link.aps.org/doi/10.1103/PhysRevMaterials.3.043606

[49] A. E. Sand, D. R. Mason, A. D. Backer, X. Yi, S. L. Dudarev, K. Nordlund, Cascade fragmentation: deviation from power law in primary radiation damage, Materials Research Letters 5 (5) (2017) 357–363. arXiv:http://dx.doi.org/10.1080/21663831.2017.1294117, doi:10.1080/21663831.2017.1294117.
URL http://dx.doi.org/10.1080/21663831.2017.1294117

[50] X. Yi, A. E. Sand, D. R. Mason, M. A. Kirk, S. G. Roberts, K. Nordlund, S. L. Dudarev, Direct observation of size scaling and elastic interaction between nano-scale defects in collision cascades, EPL 110 (3) (2015) 36001.
URL http://stacks.iop.org/0295-5075/110/i=3/a=36001

[51] R. Alexander, M.-C. Marinica, L. Proville, F. Willaime, K. Arakawa, M. R. Gilbert, S. L. Dudarev, Ab initio scaling laws for the formation energy of nanosized interstitial defect clusters in iron, tungsten, and vanadium, Phys. Rev. B 94 (2016) 024103. doi:10.1103/PhysRevB.94.024103.
URL https://link.aps.org/doi/10.1103/PhysRevB.94.024103

[52] K. Nordlund, M. Ghaly, R. S. Averback, M. Caturla, T. Diaz de la Rubia, J. Tarus, Defect production in collision cascades in elemental semiconductors and fcc metals, Phys. Rev. B 57

(1998) 7556–7570. `doi:10.1103/PhysRevB.57.7556`.
URL `http://link.aps.org/doi/10.1103/PhysRevB.57.7556`

[53] Open database of cascade damage configurations hosted by iaea.
URL `https://cascadesdb.iaea.org/`

[54] C. Hill, Summary report of the 6th biennial technical metting, in: International Atomic and Molecular Code Centres Network Meeting on Database Services for Radiation Damage in Nuclear Materials, INDC(NDS), IAEA, 2019.
URL `https://www-nds.iaea.org/publications/indc/indc-nds-0803`